Energy & Environmental Science

ROYAL SOCIETY OF CHEMISTRY

COMMUNICATION

View Article Online
View Journal | View Issue

Cite this: *Energy Environ. Sci.*, 2020, **13**, 2878

Received 13th May 2020,
Accepted 30th July 2020

DOI: 10.1039/d0ee01510e

rsc.li/ees

"Water-in-salt" polymer electrolyte for Li-ion batteries†

Jiaxun Zhang,‡[a] Chunyu Cui,‡[a] Peng-Fei Wang,‡[a] Qin Li,[a] Long Chen,[a] Fudong Han,[a] Ting Jin,[a] Sufu Liu,[a] Hema Choudhary,[a] Srinivasa R. Raghavan,[a] Nico Eidson,[ab] Arthur von Cresce,[b] Lin Ma,[b] Jasim Uddin,[c] Dan Addison,[c] Chongyin Yang *[a] and Chunsheng Wang *[ad]

Recent success in extending the electrochemical stability window of aqueous electrolytes to 3.0 V by using 21 mol kg^{-1} "water-in-salt" (WiS) has raised a high expectation for developing safe aqueous Li-ion batteries. However, the most compatible $Li_4Ti_5O_{12}$ anodes still cannot use WiS electrolyte due to the cathodic limit (1.9 V *vs.* Li/Li$^+$). Herein, a UV-curable hydrophilic polymer is introduced to further extend the cathodic limit of WiS electrolytes and replace the separator. In addition, a localized strongly basic solid polymer electrolyte (SPE) layer is coated on the anode to promote the formation of an LiF-rich SEI. The synthetic impacts of UV-crosslinking and local alkaline SPE on the anodes extend the electrochemical stability window of the solid-state aqueous polymer electrolyte to ~3.86 V even at a reduced salt concentration of 12 mol kg^{-1}. It enables a separator-free $LiMn_2O_4$//$Li_4Ti_5O_{12}$ aqueous full cell with a practical capacity ratio (P/N = 1.14) of the cathode and anode to deliver a steady energy density of 151 W h kg^{-1} at 0.5C with an initial Coulombic efficiency of 90.50% and cycled for over 600 cycles with an average Coulombic efficiency of 99.97%, which has never been reported before for an aqueous $LiMn_2O_4$//$Li_4Ti_5O_{12}$ full cell. This flexible and long-duration aqueous Li-ion battery with hydrogel WiSE can be widely used as a power source in wearable devices and electrical transportations where both energy density and battery safety are of high priority. An ultra-thick LTO electrode with UV-curable polymer electrolyte as the binder is demonstrated as a solid state battery electrode. And a high-voltage (7.4 V) solid-state bipolar cell is assembled with a solid-state UV-curable polymer as the electrolyte.

Broader context

Safety is the most important factor for rechargeable batteries especially in terms of wearable devices and electrical transportations. Aqueous electrolytes possess the merit of intrinsic safety, while the narrow (<2 V) long-duration operation voltage of traditional aqueous electrolyte is a critical bottleneck for the high energy density safety Li-ion batteries. The revolutionary "water-in-salt" electrolyte (WiSE) further broadened the long-duration operation voltage; still, most of the high capacity anodes are not workable in WiSE owing to hydrogen evolution reaction of water on the anodes. Herein, we report a polymer stabilized WiSE structure, which combined solid-state aqueous polymer electrolyte (SAPE) with a localized strongly basic solid polymer electrolyte (SPE) on the anode. The solid-state electrolyte demonstrates that the concept of a solid state battery is achievable by fabricating a high-voltage stacking cell and fabricating an ultra-thick electrode. A Li-ion battery based on capacity matched $LiMn_2O_4$/$Li_4Ti_5O_{12}$ was demonstrated to deliver an unprecedented high reversibility of charge/discharge capacities at a low current density in the battery. This newly developed reduced salt concentration WiSE not only reduces the cost of the aqueous electrolyte, but also opens up another perspective on future directions and guidance for the design of aqueous electrolytes for high-energy-density Li-ion batteries in practical applications.

Introduction

The state-of-the-art Li-ion batteries have been dominating the storage market for electronic devices and electrical vehicles owing to their high energy density of 250 W h kg^{-1} and long cycle life. However, the use of flammable non-aqueous electrolyte Li-ion batteries has raised serious safety concerns. Replacing flammable electrolytes with aqueous electrolytes will bring intrinsic safety and reduce materials and manufacturing costs. Unfortunately, aqueous Li-ion batteries suffer from low energy density due to the narrow (<2 V) electrochemical stability window (ESW) of the electrolyte. Recently, the groundbreaking "water-in-salt" electrolyte (WiSE) successfully expanded the ESW of water to 3.0 V.[1–4] To enhance the energy density of

[a] *Department of Chemical and Biomolecular Engineering, University of Maryland, College Park, MD 20742, USA. E-mail: cswang@umd.edu, cyyang@umd.edu*
[b] *Department Electrochemistry Branch, Sensor and Electron Devices Directorate, Power and Energy Division, US Army Research Laboratory, Adelphi, MD 20783, USA*
[c] *Liox Power, Inc., Pasadena, CA 91106, USA*
[d] *Department of Chemistry and Biochemistry, University of Maryland, College Park, MD 20742, USA*

† Electronic supplementary information (ESI) available. See DOI: 10.1039/d0ee01510e

‡ These authors contributed equally.

the WiSE batteries, the cathodic limitation of 1.9 V needs to be further reduced, and a high Coulombic efficiency (CE) of >99.9% at matched areal capacities of the cathode/anode at low charge/discharge rates is required for long-term cycling. To date, such a high CE has not been achieved in 3 V-class full cells, *e.g.* $LiMn_2O_4$//$Li_4Ti_5O_{12}$.

The effective strategies for suppressing a parasitic reaction on the electrodes in WiSE are (1) reducing water activity by minimizing the water molecules in the Li^+ ion solvation shell in the bulk electrolytes and (2) passivating the anode by forming an LiF-rich solid electrolyte interphase (SEI) from the reduction of LiTFSI salt.[1,5] However, due to the solubility limitation,[6] further reducing the water molecules in the Li^+ ion solvation shell is quite a challenge. For this aspect, adding a highly hydrophilic polymer network as a water stabilizer can further extend the thermodynamic stability window of WiSE and reduce the decomposition kinetics of water.[7] The molecular dynamics study of polymer–water interaction in hydrogels demonstrated that the mobility of water molecules is significantly lowered around polymer chains.[8] The NMR characterization also confirmed that the water component appears to be tightly bound to the cross-linked polymer networks.[9] The suppressing of water molecule mobility in the cross-linked polymer network will reduce the water activity, thus extending the stability window.

UV-curing is a mature polymerization technique and has been widely utilized in the domain of photolithography for the production of optical and electronic devices, biomedical applications and energy storage systems[10–12] as it is simple, low cost, fast and reliable.[13] Under UV irradiation, a liquid polyfunctional monomer reacts with a proper photo-initiator forming a solid cross-linked film. UV-cured methacrylic membranes were used as GPEs for lithium ion batteries several years ago.[14,15] Flexible 3D networks have been fabricated using the UV-curing technology, which have shown great potential for large scale applications.

In this work, by incorporating WiSE with a UV-curable methacrylic polymer, we design a solid-state aqueous polymer electrolyte (SAPE), in which the abundant hydrophilic groups stabilized the water molecules due to the sluggish water mobility in SAPE and formed a water-less thin passivation interphase between the anode and electrolyte. Moreover, the anode was pre-coated with a strongly basic water-free solid polymer electrolyte to further promote the formation of a passivation interphase.[16] All of these promoted the formation of a more robust SEI to reduce the water reduction reactions on the anode surface. The electrochemical stability window of aqueous electrolytes was extended from 3.0 V of 21m WiSE to ~3.86 V of 12m UV-cured SAPE. Using a 3 V class $LiMn_2O_4$//$Li_4Ti_5O_{12}$ (LMO//LTO) full cell with a capacity ratio Q_c/Q_a of 1.14 and an areal capacity of 0.5 mA h cm^{-2} as a demo cell, the UV-cured SAPE enables the LMO//LTO full cell to achieve an energy density of 151 W h kg^{-1} at 0.5C with an initial Coulombic efficiency of 90.50% and cycled for over 600 cycles with an average Coulombic efficiency of 99.97%.

Results and discussion

Synthesis and properties of SAPEs

The synthetic procedure of the solid-state aqueous polymer electrolytes is demonstrated in Fig. 1a. A methacrylic based di-functional oligomer, bisphenol A ethoxylate dimethacrylate (BEMA, M_w = 1700), was used as a cross-linker.[15] Poly(ethylene glycol)methyl ether methacrylate (PEGMA, M_w = 500) was used as a reactive diluent to enhance the mobility of lithium ions in the polymer matrix.[15] 2-Hydroxy-2-methylpropiophenone (HMPP) functioned as a photo-initiator. Firstly, the precursor solution was prepared by dissolving different salts (LiTFSI, LiOTf, Pyr_{13}TFSI) into water and monomers (Fig. 1a). The precursor solution is transparent due to the miscibility between water, monomers and salts. Then, the precursor solution was cross-linked by exposing it to UV light (wavelength ~400 nm) for 90 s to induce the photopolymerization of the methacrylic groups and form a solid-state aqueous polymer electrolyte (SAPE) (Fig. S1, ESI†). The crosslinking process is realized by the conversion of the double bond (>C=C<) during exposure to UV light (Fig. 1a). As a one-pot synthetic method, the UV-cured polymerization is a facile and highly efficient process. Two types of SAPEs were fabricated. One is a 11m LiTFSI–LiOTf–H_2O–polymer SAPE (11m SAPE) that is obtained by dissolving 8.5m LiTFSI and 2.5m LiOTf into monomers and water (m is mol kg^{-1}). The second type SAPE is a 12m LiTFSI–LiOTf–Pyr_{13} TFSI–H_2O–polymer SAPE (12m SAPE) that is achieved by dissolving 5.2m LiTFSI, 5m Pyr_{13} TFSI and 1.8m LiOTf into monomers and water. LiTFSI and LiOTf facilitate the formation of a hydrophobic LiF SEI.[17] Since Pyr_{13} TFSI is non-volatile and non-flammable,[18] it was introduced into 12m SAPE to further lower the water activity and change the solvation structure around Li^+.[19] The detailed weight ratio of each component in the system is presented in Table S1 (ESI†).

The thermal stability of 11m SAPE and 12m SAPE was evaluated using differential scanning calorimetry (DSC), and compared to 28m (21mLiTFSI–7m LiTOf) liquid WiSE. Both SAPEs show high thermos-stability with no significant exothermic peak observed before 350 °C, which is essentially identical to that of 28m WiSE (Fig. S2, ESI†). Moreover, water-retention in 12m SAPE is evaluated under real ambient conditions (room temperature). As shown in Fig. S3 (ESI†), the mass of 12m SAPE gradually increases during the first few hours, owing to the moisture abstraction from the ambient air (the air humidity was around 60%). After this the weight remains constant. Thus, the 12m SAPE has a superior ability to maintain water inside of the polymer framework even under the ambient environment.

The ionic conductivities of 28m WiSE, 11m SAPE and 12m SAPE at various temperatures are presented in Fig. 1c. At room temperature (25 °C), the ionic conductivities of 28m WiSE, 11m SAPE and 12m SAPE are 7.5 mS cm^{-1}, 3.0 mS cm^{-1} and 1.7 mS cm^{-1}, respectively. Although the ionic conductivities of 11m SAPE and 12m SAPE at room temperature are slightly lower than those of the non-aqueous electrolyte (10.7 mS cm^{-1} for 1.0 M $LiPF_6$ in EC/DMC at 25 °C[20]) and the liquid WiSE electrolyte (10.0 mS cm^{-1} for 21m LiTFSI in water at 25 °C[1]), they are still 2 orders of magnitude larger than those of the best

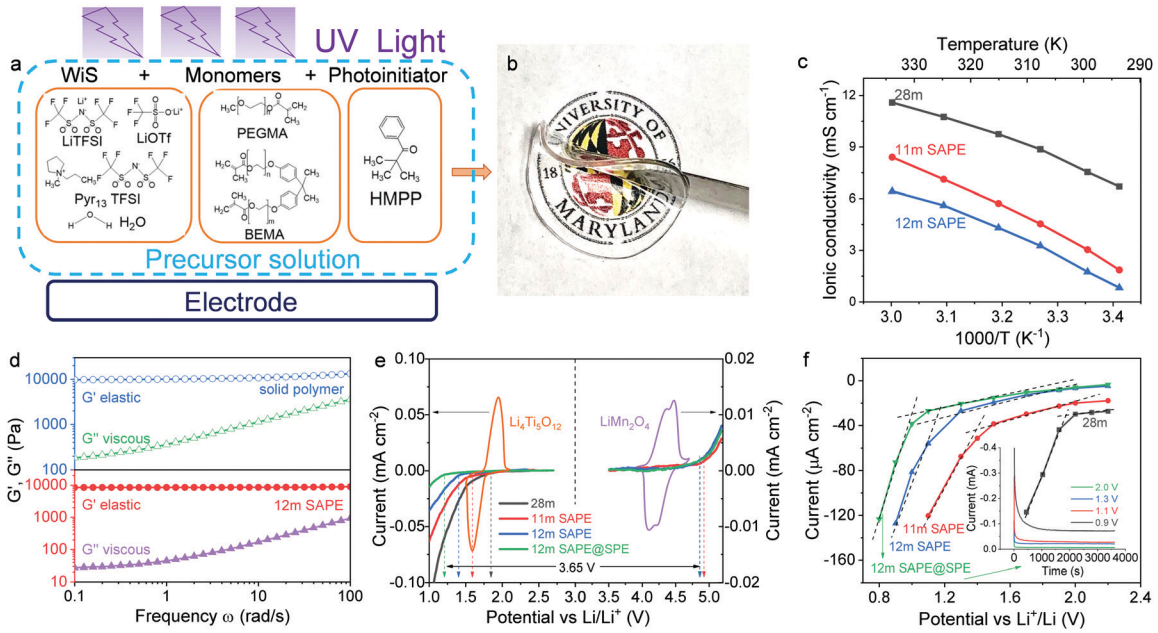

Fig. 1 Schematic of the SAPE synthetic procedure and properties of the synthesized SAPEs. (a) Chemical structure of the compositions used to synthesize solid-state aqueous polymer electrolyte networks. And schematic exemplifying the concept of *in situ* crosslinking on an electrode. (b) Prototype of a typical SAPE network. (c) The temperature dependence of ionic conductivities in the range of 20 to 60 °C for 28m WiSE, 11m SAPE and 12m SAPE. (d) Oscillatory shear rheology of the solid polymer and 12m SAPE, the elastic modulus G' and the viscous modulus G'' are plotted as functions of the frequency ω. (e) The linear sweep voltammetry of different electrolytes (28m WiSE, 11m SAPE, 12m SAPE) at a scanning rate of 0.1 mV s^{-1}. (Electrode area: 0.5 cm^2) PEO–LiTFSI–KOH SPE is coated on an Al foil electrode to measure the cathodic limit for the 12m SAPE@SPE electrolyte. The working electrodes were Al for the cathodic limit and Ti for the anodic limit. Cyclic voltammetry (CV) of $Li_4Ti_5O_{12}$ (LTO) and Li_2MnO_4 (LMO) scanned at 0.1 mV s^{-1} in 12m SAPE is also presented. (f) Chronoamperometry of different electrolytes (28m WiSE, 11m SAPE, 12m SAPE and 12m SAPE@SPE electrolyte) on an Al foil electrode. Different potentials are applied on the Al working electrode, with the steady state current shown in one curve. The current–time curve of the 12m SAPE@SPE electrolyte is presented in the inset.

solid polymer electrolytes (4.4×10^{-5} S cm^{-1} for SiO_2 modified PEO-$LiClO_4$ SPE at 30 °C).[21,22]

The mechanical properties of the solid-state aqueous polymer electrolyte (12m SAPE) were studied by oscillatory shear (detailed in the ESI†),[23] and compared with the solid polymer (10 wt% BEMA and 90 wt% PEGMA). Fig. 1d presents the frequency (ω) response of the elastic modulus G' and viscous modulus G''. The elastic modulus G' of both SAPE and the solid polymer are much larger than their viscous modulus G''. In addition, the modulus G' is independent of frequency and G'' is gradually increased with frequency (ω), suggesting that the SAPE is more like solid electrolytes rather than the liquid electrolytes. The value of elastic modulus G' is a crucial parameter as it is the modulus of the polymer under shear (in the linear viscoelastic region). G' of the solid polymer is 10 kPa, and G' of 12m SAPE is 8.5 kPa (both values apply to a frequency of 1 rad s^{-1}). The elastic modulus of 12m SAPE is very close to that of the solid polymer, and is high enough to use as a separator to prevent the contact of the anode and cathode electrode. As depicted in Fig. S4 and Video S1 (ESI†), SAPE exhibits good stretchability even after the length of SAPE is extended to nearly 200%, demonstrating excellent flexibility of the SAPE.

The electrochemical stability windows of 28m WiSE, 11m SAPE, and 12m SAPE are compared by linear sweep voltammetry (LSV) at a scanning rate of 0.1 mV s^{-1} using non-active titanium (Ti) foil or aluminum (Al) foil as current collectors. As shown in Fig. 1e and Fig. S5a (ESI†), the hydrogen evolution potentials of 28m WiSE, 11m SAPE and 12m SAPE are 1.83 V, 1.59 V and 1.41 V, respectively. Therefore, the cathodic limit of a 11m SAPE electrolyte negatively extends by 0.24 V due to the high salt concentration and polymer framework as a water stabilizer. The further extension of ESW for 12m SAPE is due to the cooperation of the high lithium salt concentration, polymer framework and ionic liquid. Besides, a strongly basic water-free polymer electrolyte was pre-coated on Al foil to further expand the electrochemical stability window (ESW) of 12m SAPE. The pre-coated solid polymer electrolyte (SPE) composed of PEO, LiTFSI and KOH with the weight ratio of 0.55 : 0.25 : 0.2, is denoted as SPE. The hydrogen evolution potential on Al after SPE coating is further negatively shifted to 1.21 V. To eliminate kinetic effects, stricter ESW measurements using chronoamperometry are conducted. Specifically, a constant potential is imposed on the working electrode and the current is recorded with time until the current reaches a steady state. The current–time curves of Al electrodes at different potentials in 28m WiSE, 11m SAPE and 12m SAPE are presented in Fig. S5 (ESI†). At the steady state, the onset of rapidly raising current is only attributed to the side reaction of the hydrogen evolution reaction (HER). The cathodic limit of 12m SAPE@SPE can be negatively extended to 1.0 V from the chronoamperometry analysis (Fig. 1f). The extension of the cathodic limit is due to the suppression of water molecule

activities within the cross-linked solid-state polymer network and highly-concentrated salt as discussed in the following section. The anodic limits of 11m SAPE and 12m SAPE are 4.87 V and 4.86 V, respectively, which is 4 mV less than 28m WiSE due to the oxidation of the solid polymer electrolyte at high voltage (Fig. 1e).[15] Overall, an electrochemical stability window of 3.86 V was achieved for the 12m SAPE@SPE electrolyte. Since the redox reaction potentials of the LMO cathode and LTO anode shifted ~200 mV positively in the high concentration electrolyte, the redox reaction potentials of LMO and LTO are completely inside of the ESW of 11m SAPE, 12m SAPE, and 12m SAPE@SPE electrolytes, which will potentially achieve high CEs.

High reversibility of LTO in solid-state aqueous polymer electrolytes

Fig. 2a shows a schematic diagram of the LMO/SAPE@SPE/LTO cell, and Fig. 2b shows the cross-section SEM image of the LMO/12m SAPE@SPE/LTO cell. The CE of LTO in different electrolytes is evaluated using excess LMO as the counter electrode (LMO//LTO capacity ratio of 3 : 1) in coin cells. As presented in Fig. 2c, the CE of LTO at the second cycle in 28m WiSE is only 59% owing to the rapid side reaction of the hydrogen evolution reaction (HER). After introduction of a polymer into water-in-salt electrolyte to form the solid-state aqueous polymer electrolyte, the CE of LTO in 11m SAPE and 12m SAPE increases to 93.6% and 98.9% after 10 cycles, respectively. The introduction of the PEO–LiTFSI–KOH SPE layer between LTO and 12m SAPE electrolyte further enhances the CE of LTO to 99.6% after 10 cycles, indicating that the side reaction of HER on LTO is effectively suppressed by the PEO–LiTFSI–KOH SPE layer. In order to quantitatively study the HER during the cycling of the LMO//LTO full cell, an *in situ* cell pressure analysis is performed (Fig. 2d). The increase in cell pressure during charge/discharge cycles demonstrates the production of hydrogen gas inside of the cell, which is confirmed using mass spectrometry analysis. The cell pressure increased rapidly in 28m WiSE, while the increase of the cell pressure in 12m SAPE and 12m SAPE@SPE electrolytes is very slow, especially in 12m SAPE@SPE electrolyte. The gas composition of 12m SAPE@SPE electrolyte was analyzed using mass

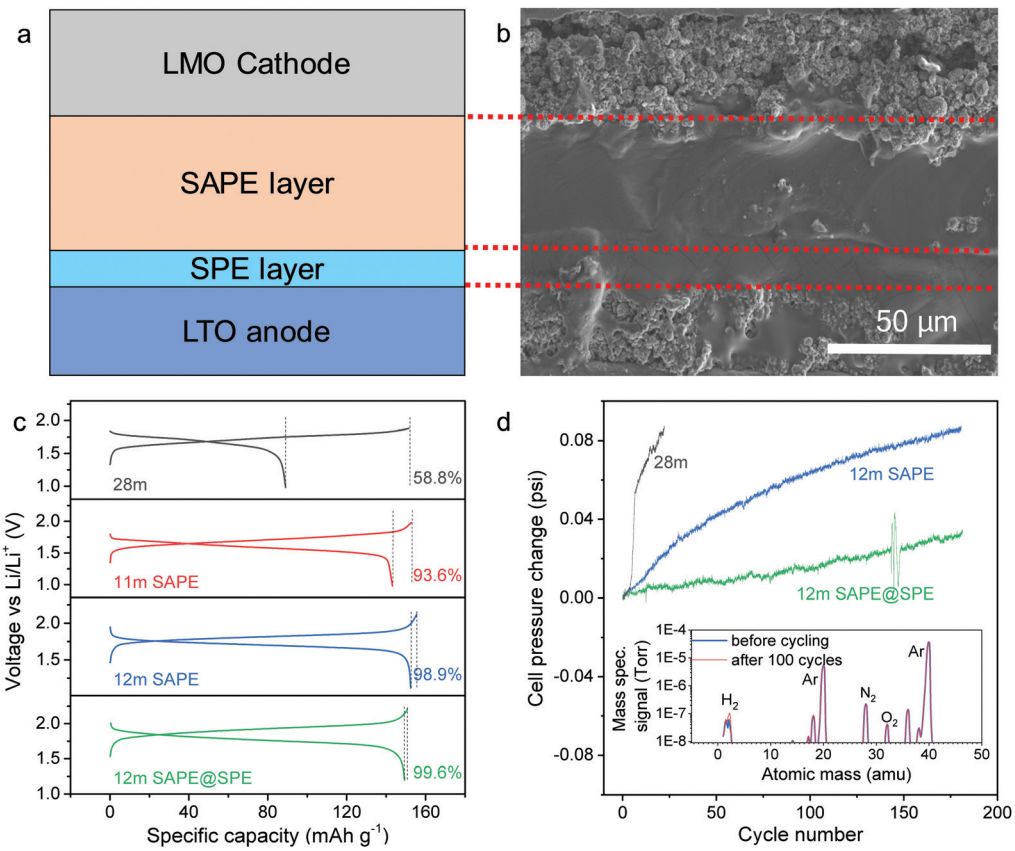

Fig. 2 Schematic and reality of the LMO//LTO full cell structure, Coulombic efficiency of an LTO anode and *in situ* monitoring of internal gas pressure change for the full cell. (a) Schematic structure of an LMO/SAPE layer/SPE layer/LTO cell. (b) Cross-section SEM image of an LMO//LTO full cell with 12m SAPE and PEO–LiTFSI–KOH SPE layer (LMO anode (~35 μm); SAPE layer (~42 μm); SPE layer (~8 μm); LTO anode (~28 μm)). (c) Voltage profiles for the 10th cycle charge–discharge profiles (0.5C) of full cells constructed with the Li_2MnO_4 cathode and $Li_4Ti_5O_{12}$ anode in 28m WiSE (2nd cycle), 11m SAPE, 12m SAPE and 12m SAPE@SPE electrolytes. The capacity ratio of LMO//LTO is set as 3 : 1, the Coulombic efficiency of the full cell is presented as the efficiency of the LTO anode. (d) *In situ* monitoring of internal gas pressure change for the LMO//LTO full cell with various electrolytes during long cycling, revealing the amount of H_2 gas evolution. Inset: The gas compositions examined using mass spectrometry before and after cycling for the LMO//LTO full cell with 12m SAPE@SPE electrolyte.

spectrometry. Comparing the gas composition in the fresh cell and in the cell after 100 cycles in 12m SAPE@SPE electrolyte, only hydrogen gas increased, indicating that the increase of cell pressure during cycling is contributed by the HER. The increase of pressure in SAPE@SPE electrolyte is mainly attributed to hydrogen evolution during the SEI formation process in the initial 10 cycles. It should be noted that a very small amount of H_2 is generated in 100 cycles (7.6×10^{-8} mol mA h^{-1}), which is comparable with the gas amount generated in state-of-the-art non-aqueous LMO//LTO full cells during cycling.[24]

The mechanism for the suppression of the hydrogen evolution reaction was investigated using Fourier transformed infrared (FTIR), Raman and X-ray photoelectron spectroscopies (XPS). The water activities in 11m and 12m SAPE and methacrylic based solid polymer are characterized using FTIR spectroscopy. Fig. 3a presents the FTIR spectra of water in the solid polymer (10 wt% BEMA and 90 wt% PEGMA) to demonstrate the O–H stretching vibration modes of water molecules, which reveals their hydrogen bond association.[2,25] As a reference, the FTIR spectra of pure water present fine structures of the featured broad band, consisting of several components attributed to various water molecules with different hydrogen-bonding environments in water clusters.[2,6,25] Specifically, the O–H stretching band can be deconvoluted into several Gaussian peaks corresponding to hydrogen-bonded water molecules with different donor (D) and acceptor (A) hydrogen bonds. The FTIR spectra of H_2O can be deconvoluted into five sub-bands, located at 3028, 3225, 3405, 3551 and 3637 cm^{-1}, which are assigned to the O–H vibrations engaged in DAA, DDAA, DA, and DDA hydrogen-bonding and free O–H vibrations. The FTIR spectra of the solid polymer with 6% and 10% water were first analyzed as a control electrolyte to compare with the SAPE. For the solid polymer with 10% water, three Gaussian peaks centered at 3278, 3458 and 3561 cm^{-1} are assigned for deconvolution of this area. The position of the bands at 3278 cm^{-1} and 3458 cm^{-1}, corresponding to DDAA and DA stretching vibrations, is slightly shifted in respect to the peaks of water. The peak centered at around 3561 cm^{-1} represents the superposition of DDA and free O–H stretching vibration. The disappearance of DAA and weakening of the free O–H stretching vibration demonstrates that the polymer matrix successfully stabilizes the water molecules, dramatically depressing the activity and mobility of the water molecules. The stretching vibrations of the solid polymer with 6% water are similar to that of the solid polymer with 10% water, but the peak position moved closer to the stretching vibration of DA, which indicates that large water clusters are reduced.[26]

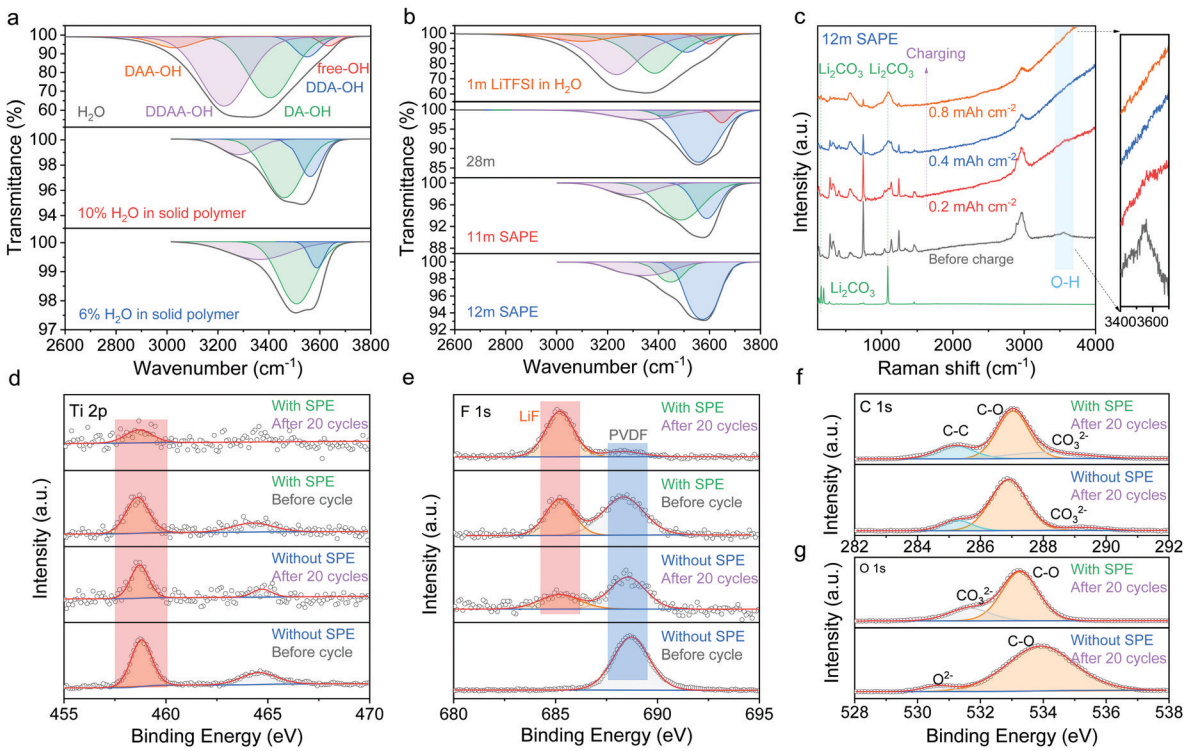

Fig. 3 FTIR characterizations of the electrolyte, Raman and XPS characterizations of SEI between the anode and electrolytes. (a and b) The FTIR spectra observed in the range of 2600–3800 cm^{-1} correspond to the O–H stretching modes of water molecules. The O–H stretching bands were broken down into Gaussian peaks supposedly corresponding to hydrogen-bonded water molecules with different donor and acceptor hydrogen bonds. (c) *In situ* Raman spectra of the 12m SAPE/FTO anode interface at 1.7 V, showing spontaneous formation of a water-less passivation layer and accumulation of Li_2CO_3 as a major composition of the SEI layer. The interface was simulated by applying a constant voltage (1.7 V *vs.* Li/Li^+) on fluorine doped tin oxide (FTO) glass as a transparent electrode. (d–g) XPS Ti 2p, (d) F 1s, (e), C 1s (f), and O 1s (g) spectra of the LTO anode before cycling and after 20 cycles with 12m SAPE or 12m SAPE@SPE as the electrolyte, showing the detailed composition of the SEI layer (LiF, Li_2CO_3). The solid polymer electrolyte layer and SAPE were carefully removed.

The FTIR spectra of different aqueous electrolytes in Fig. 3b show typical stretching modes of the O–H vibration peak (3000–3800 cm^{-1}). The 1m LiTFSI in H_2O shows a similar spectrum to pure water, which can be deconvoluted into five sub-bands,[27] located at 3156, 3251, 3397, 3512, and 3612 cm^{-1} (H_2O), which are assigned to O–H vibrations engaged in DAA, DDAA, DA, and DDA hydrogen-bonding, and free O–H vibrations. The blue shift of the O–H covalent bond oscillation is attributed to the perturbation of a water hydrogen bond network with lithium salt around it. For the 28m WiSE, four Gaussian peaks can be deconvoluted in this area. The disappearance of DAA stretching vibrations at 3028 cm^{-1} verified that mobility of the water molecules is constrained within the 28m highly-concentrated salt aqueous electrolyte. Three Gaussian peaks can be deconvoluted for the 11m SAPE and 12m SAPE, compared with 28m WiSE, low-frequency portions' demise to high-frequency ones in 12m SAPE, indicating that the oxygen groups on the polymers further break down the water-rich cluster size[28] and reduce the activity of the water molecules. Furthermore, Raman spectra are adopted to characterize the structure of the aqueous electrolytes. As summarized in Fig. S6a (ESI†), the O–H vibration peak at 3560 cm^{-1} gradually disappears from 28m WiSE to 12m SAPE, which is in accordance with the FTIR results. Consequently, the water activity is severely reduced in 12m SAPE under the cooperation of a cross-linked solid-state polymer network and highly-concentrated salt, and then the CE will be greatly improved.

In addition to the reduction of water activity by salt and polymer, a solid electrolyte interphase (SEI) also formed on the anode in WiSE due to the reduction of salt as reported before.[29] Raman spectroscopy was used to monitor the water reduction and SEI formation on a transparent fluorine doped tin oxide (FTO) glass anode coupled with a $LiMn_2O_4$ (>3 mA h cm^{-2}) counter electrode. The FTO anode in the FTO/SAPE/LMO cell is discharged at a constant potential of 1.7 V (*vs.* Li/Li^+) to mimic the LTO anode in the LMO//LTO cell, while a Raman beam is focused on the interface at FTO/SAPE to *in situ* monitor water consumption and SEI formation. Fig. 3c shows the *in situ* Raman spectra of the 12m SAPE/FTO interface. The Raman laser is set to focus on the FTO/12m SAPE interface. The pristine sample (before charging) presents a featured band (~3560 cm^{-1}, similar to the FTIR results) of water. After being charged to 0.8 mA h cm^{-2}, the water signal totally disappeared. Therefore, the side reaction (water decomposition) in the initial cycle consumes the water in the interface layer of 12m SAPE, forming a water-less thin passivation interface on the electrode and extending the window. Meanwhile, a peak of Li_2CO_3 is detected at the interface as charging proceeds, which can be attributed to the formation of SEI on FTO. The formation of water-less thin Li_2CO_3 SEI during the first charge enhanced the Coulombic efficiency. Still, the formation of this water-free layer in the initial cycle would consume Li^+ ions from the cathode in a full cell, which compromised the overall capacity. To enhance this strategy, a basic water-free PEO–LiTFSI–KOH SPE layer pre-coated on the anode can further reinforce the Coulombic efficiency and the high local pH can also promote the LiTFSI reduction forming LiF SEI.[16]

XPS was used to further investigate the SEI composition formed on the surface of the LTO anodes in the LMO//LTO full cells using 12m SAPE with and without PEO–LiTFSI–KOH SPE coating. The LTO with the PEO–LiTFSI–KOH SPE layer coating is denoted as 'With SPE', and the one with no SPE pre-coating is denoted as 'Without SPE'. For the LTO without SPE layer, the Ti 2p XPS peak signal at 458.6 eV is very strong before cycling and the peak intensity becomes weak after 20 charge/discharge cycles. The Ti 2p XPS peak at 458.6 eV corresponds to Ti in the LTO electrode material, which indicates that the surface of the LTO anode is covered by SEI after cycling (Fig. 3d). From the F 1s XPS peak (Fig. 3e), a peak at 685.2 eV corresponding to F^- in LiF is detected after cycling, while a peak at 688.5 eV results from the PVDF binder in the composite electrode. Meanwhile, a peak of C 1s at 288.9 eV corresponds to CO_3^{2-} that is also formed on the LTO surface (Fig. 3f), which is consistent with Raman analysis that Li_2CO_3 SEI is also formed on the LTO surface. The formation of LiF-Li_2CO_3 SEI can effectively extend the electrochemical stability window of WiSE.[29]

When a water-free basic SPE layer (PEO–LiTFSI–KOH) was coated on the LTO anode, the Ti 2p XPS peak signal is weaker than the LTO without SPE layer coating (Fig. 3d), which means that something derived from the SPE layer remained on the LTO anode. Interestingly, the F 1s XPS peak at 685.2 eV corresponding to LiF is detected before cycling, which suggests that LiF immediately forms on the LTO anode upon the coating of a basic water-free SPE layer without any electrochemical process. It has been reported by Dubouis *et al.*[16] that hydroxides can chemically react with TFSI anions through a nucleophilic attack process and catalyze the formation of a fluorinated solid electrolyte interphase. Thus, the existence of KOH contributes to the decomposition of LiTFSI in the formation of LiF on the anode surface. After 20 cycles, the Ti 2p XPS peak signal virtually vanished, illustrating that the surface of LTO is completely covered by SEI. Simultaneously, the F 1s XPS peak signal at 688.5 eV that stems from the PVDF binder in the composite electrode also vanished. A very strong F 1s XPS peak signal at 685.2 eV corresponding to LiF is presented, indicating the formation of massive LiF on the surface of LTO. At the same time, the C 1s peak at 288.9 eV and O 1s peak at 531.6 eV correspond to metal carbonates (Li_2CO_3), which is in agreement with the research before.[30,31] The Li 1s XPS peak signal is presented in Fig. S6b (ESI†). A peak at 56.18 eV is close to the binding energy of LiF, another peak at 55.43 eV is close to the binding energy of Li_2CO_3. Thus, the Li 1s XPS signal further confirmed the existence of LiF and Li_2CO_3 in the SEI layer. Combining the XPS result of Ti 2p signal, a dense SEI layer composed of LiF and Li_2CO_3 is formed on the surface of the LTO anode. As reported in previous research,[32,33] dense and robust LiF SEI on the LTO surface can block the water molecules effectively. Moreover, the LiF–Li_2CO_3 composite has a much better Li-ion conductivity than LiF and Li_2CO_3.[29] Accordingly, with the incorporation of these two compositions in the SEI, the Coulombic efficiency of the LTO anode was enhanced significantly. Also, as presented in Fig. 3f and g, the SEI layer is composed of some organic compounds containing C–O and

C–C groups, which originate from the reduction of the polymer on the anode surface.

Electrochemical performance of the capacity matched full cell

The LMO//LTO full Li-ion cell with a practical capacity ratio (LMO/LTO) of 1.14 and an areal capacity of 0.5 mA h cm^{-2} is assembled to evaluate the electrochemical performance in different electrolytes. The slightly higher capacity of LMO than that of LTO is to compensate the irreversible Li consumption during the formation of SEI in the initial cycles. Here, we utilize a low rate of 0.5C to evaluate the authentic stability of the aqueous electrolyte. The cycling performances of the LMO//LTO full cell with 28m WiSE, 11m SAPE, 12m SAPE and 12m SAPE@SPE electrolytes are presented in Fig. 4a and b and Fig. S7 (ESI†). The discharge capacity of the LMO//LTO full cell decays rapidly to 37% of the initial capacity after 5 cycles in 28m WiSE owing to the low Coulombic efficiency (<70%). With the incorporation of polymer, the discharge capacity of the LMO//LTO full cell in 11m SAPE decreased to 100 mA h g^{-1} (of LTO mass) after 20 cycles. The discharge capacity of the LMO//LTO full cell in 12m SAPE was found to remain at 125 mA h $g^{-1}_{(LTO)}$ after 100 cycles, with a high CE of 99.8%. For the LMO//LTO full cell with 12m SAPE@SPE electrolyte, the highest discharging capacity of 158 mA h $g^{-1}_{(LTO)}$ was achieved. The high CE of 90.5% in the first cycle is attributed to the *in situ* formation of SEI layer on the LTO anode. To the best of our knowledge, this is the highest initial CE compared to the state-of-the-art aqueous electrolyte full cell systems reported so far. The dense SEI components formed in the first several cycles stabilize the LTO surface, and enable the CE to be increased to nearly 99.9% after only 20 cycles (Fig. 4b). After 200 cycles, the discharge capacity remains at ~142 mA h $g^{-1}_{(LTO)}$, with the CE reaching 99.95%, showing an excellent cycling stability. The corresponding voltage profiles of the LMO//LTO full cell in 12m SAPE@SPE electrolyte are shown in Fig. 4c. The charge–discharge curve of the LMO//LTO full cell in 12m SAPE@SPE electrolyte is the same as the behavior of LMO//LTO in non-aqueous electrolyte,[34] of which a voltage plateau at 2.5 V/2.6 V is observed during the discharging/charging processes, respectively. The LMO//LTO full cell with 12m SAPE@SPE electrolyte achieves a high energy density of 151 W h kg^{-1} (60.5 A h kg^{-1}, 2.5 V average discharge potential) based on the total mass of LMO and LTO, and maintained 131 W h kg^{-1} (54.5 A h kg^{-1}, 2.4 V average discharge potential) even after 200 cycles (Fig. S8, ESI†). At a high C rate (1C), the LMO//LTO full cell shows exceptional cycling stability with a capacity decay rate per cycle of 0.034% for 600 cycles, with an average CE of 99.97%, which is comparable to non-aqueous Li-ion cells.[35] Here, we present the optimization process of monomers' weight ratio and Pyr_{13}TFSI's molar ratio within the SAPE electrolyte in Fig. S9, S10 and Tables S2, S3 (ESI†).

The rate capability of the LMO//LTO full cell with 12m SAPE or 12m SAPE@SPE electrolyte is evaluated in Fig. 4e. At a low rate of 0.2C, the discharge capacity of the LMO//LTO full cell with 12m SAPE reached 160 mA h $g^{-1}_{(LTO)}$. However, the low CE of 95% causes a quick capacity decay, which is different from

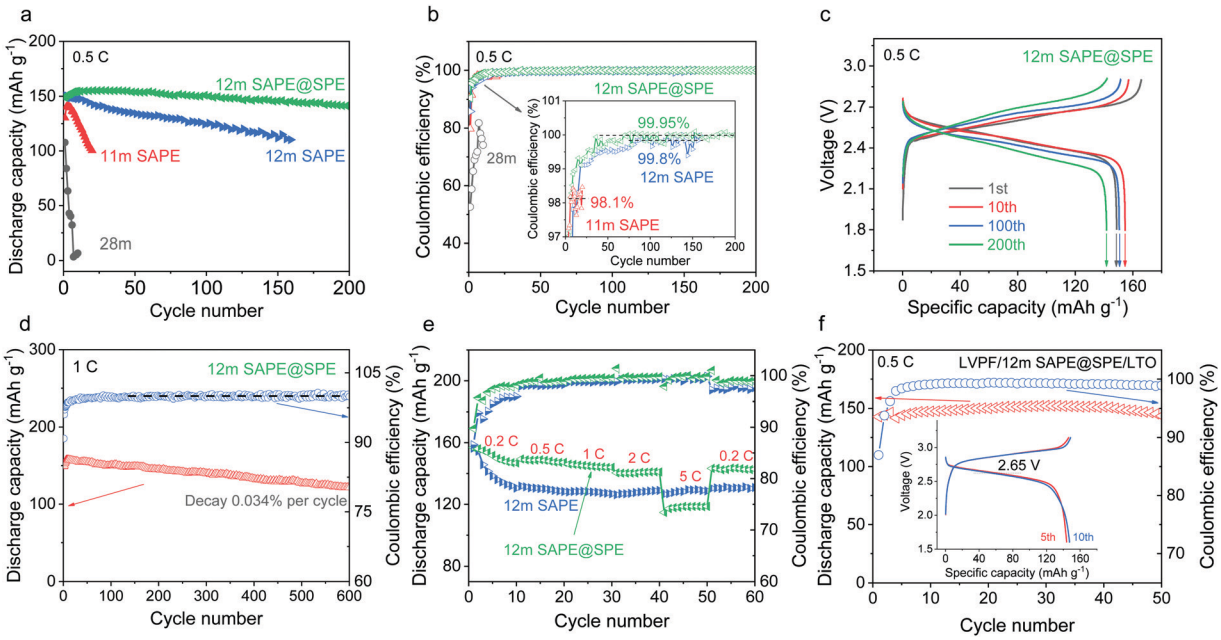

Fig. 4 Electrochemical performance of the capacity matched LMO//LTO full cell and LVPF//LTO full cell. Cycling stability (a) and Coulombic efficiency (b) of the LMO//LTO full cell in 28m WiSE, 11m SAPE, 12m SAPE and 12m SAPE@SPE electrolytes at 0.5C. (c) The voltage profiles of the 1st, 10th, 100th and 200th cycles of the LMO//LTO full cell in 12m SAPE@SPE electrolyte at 0.5C (0.075 A g^{-1} for LTO, based on mass of LTO). (d) Cycling stability and Coulombic efficiency of the LMO//LTO full cell in 12m SAPE@SPE electrolyte at 1C. (e) The rate capability of the LMO//LTO full cell in 12m SAPE and 12m SAPE@SPE electrolytes at room temperature. (f) Cycling stability, Coulombic efficiency and voltage profiles (inset) of the LVPF//LTO full cell in 12m SAPE@SPE electrolyte at 0.5C.

the capacity behavior of LMO//LTO at a high rate of 0.5C (Fig. 4a) where the capacity is slightly low (150 mA h g^{-1}), but cycling is more stable. Therefore, the SEI is more easily formed at a relatively high rate. With the increase of current density, the LMO//LTO full cell with 12m SAPE maintains the discharge capacity of 130 mA h $g^{-1}_{(LTO)}$ at 0.5C (0.075 A g^{-1}) and 127 mA h $g^{-1}_{(LTO)}$ at 2C (0.3 A g^{-1}). In sharp contrast, the LMO//LTO full cell with 12m SAPE@SPE electrolyte delivers a much higher CE at 0.2C, and a discharge capacity of 147 mA h $g^{-1}_{(LTO)}$ after 10 cycles presents at 0.2C. With increase in the current density, it maintained a discharge capacity of 147 mA h $g^{-1}_{(LTO)}$ at 0.5C (0.075 A g^{-1}) and 141 mA h $g^{-1}_{(LTO)}$ at 2C (0.3 A g^{-1}), which are much higher than that of 12m SAPE. After the rate capability recovered to 0.2C (0.03 A g^{-1}), the discharge capacity returned to 144 mA h $g^{-1}_{(LTO)}$ revealing an excellent rate performance, much better than the typical solid polymer electrolyte in full cells.[21]

To fully use the high anode potential limit (4.86 V) of the solid-state aqueous polymer electrolyte system, high potential $LiVPO_4F$ (LVPF) was used as a cathode to couple with LTO. The electrochemical performance of the LVPF//LTO full Li-ion cell with an areal capacity of 0.5 mA h cm^{-2} and P/N capacity ratio of 1.4 is evaluated at 0.5C in 12m SAPE@SPE electrolyte. The cycling performances and voltage profiles are presented in Fig. 4f. The capacity ratio of LVPF/LTO is 1.4. After 3 formation cycles, the discharge capacity reaches a steady value of 152 mA h g^{-1}. The Coulombic efficiency is close to 99.3% for the LVPF//LTO full cell. The discharge platform voltage is close to 2.65 V. Thus, the energy density further enhanced with the cooperation of LVPF and LTO.

The electrolyte flammability and LMO//LTO cell flexibility were also evaluated. Previous reports have proved that 28m WiSE is non-flammable, and the ion liquid Pyr_{13} TFSI exhibits both non-volatility and non-flammability.[18] As revealed in Fig. S11 and Video S2 (ESI†), after removing the fire from the 12m SAPE sample, the electrolyte won't continue combusting, presenting an excellent safety performance owing to the intrinsically safe nature of water. As shown in Fig. S12a (ESI†), the LMO//LTO cell holds almost the same capacity after bending the cell to 45°, 90°, 135° and 180°, and negligible capacity is lost even after bending the cell over 200 times (Fig. S12b, ESI†), confirming the excellent flexibility. Video S3 (ESI†) shows the robustness of the LMO//LTO cells under ambient air and water environments. As revealed, the flexible pouch cell with a capacity of 100 mA h (Fig. S13, ESI†) successfully powered a mini-fan, which requires a power of around 160 mW.

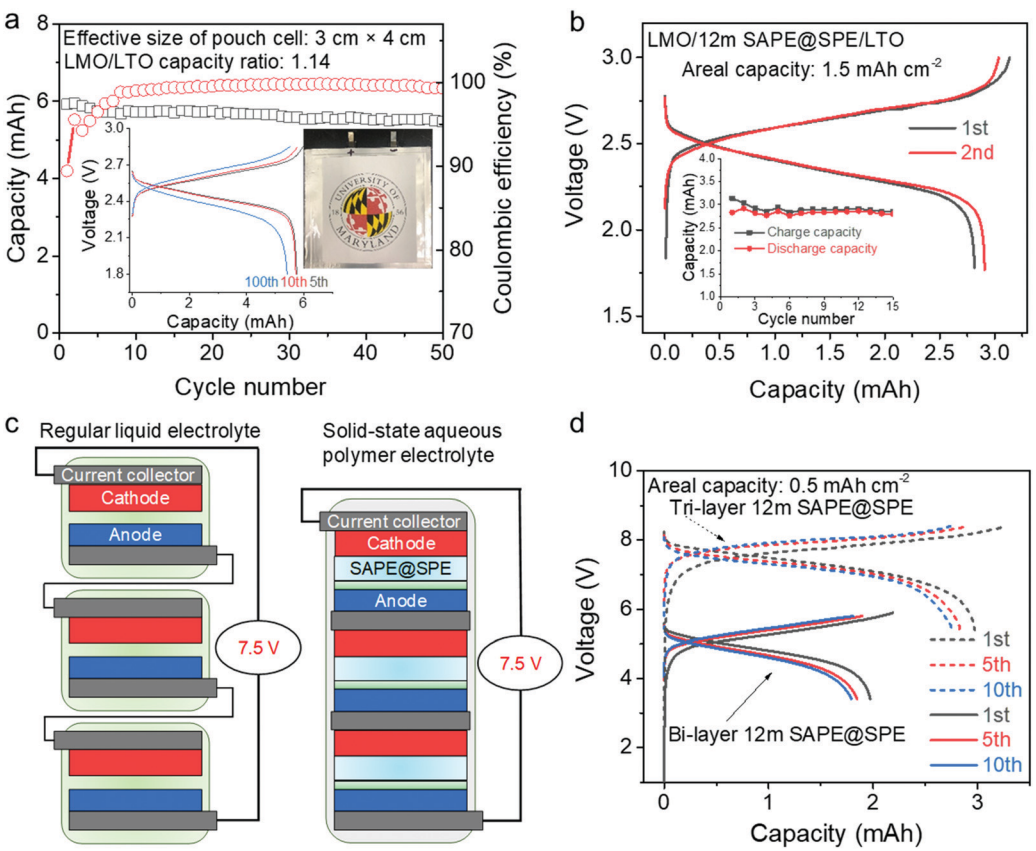

Fig. 5 Electrochemical performance of a large scale LMO//LTO full cell, high active material loading full cell and bipolar cell. (a) Cycling stability, Coulombic efficiency and voltage profiles (inset) of the LMO//LTO pouch cell in 12m SAPE@SPE electrolyte at 0.5C. (b) Cycling stability (inset) and voltage profiles of the LMO//LTO full cell with loading amount of 1.5 mA h cm^{-1} active material in 12m SAPE@SPE electrolyte at 0.2C. (c) Schematic structure of a tri-layered bipolar stacked LMO//LTO cell. (d) The voltage profiles of a bi-layered and tri-layered bipolar LMO//LTO coin cell with 12m SAPE@SPE electrolyte at 0.2C.

Moreover, after the flexible pouch cell was cut in ambient air and water, no catastrophic cell failure was detected, and the fan kept working. Benefiting from the strong bonding of the polymer network, which keeps the water and salt in the framework of the polymer, the aqueous SAPE can withstand cutting and continue to operate under an open cell condition even in a water environment without failure. The outstanding safety performance of this newly developed aqueous electrolyte opens a door for the application of lithium-ion batteries.

A 3 cm × 4 cm size LMO//LTO pouch cell with a capacity ratio (LMO/LTO) of 1.14 and an areal capacity of 0.5 mA h cm^{-2} is assembled to evaluate the electrochemical performance in the 12m SAPE@SPE electrolyte. The cycling performance of a large scale pouch cell is presented in Fig. 5a. A low C rate of 0.2C is applied on the pouch cell to fully use the active material for 5 cycles; after this formation process, we use 0.5C for the cycling process. A high capacity of 5.9 mA h can be reached for this pouch cell. The discharge capacity of the LMO//LTO pouch cell in 12m SAPE@SPE remained around 94% after 50 cycles. The corresponding voltage profiles of the LMO//LTO pouch cell in 12m SAPE@SPE are presented in the inset of Fig. 5a. The charge–discharge curves of the pouch cell are similar to the coin cells. To increase the energy density, we increased the loading of the active material of LMO//LTO cells to 1.5 mA h cm^{-1}. The cross-section SEM image of a high loading LTO electrode is presented in Fig. S14 (ESI†). The thickness of the LTO electrode is around 86 μm. The electrode area is 1.98 cm^2. The electrochemical performance is shown in Fig. 5b. The voltage profiles of the high loading LMO//LTO full cell in 12m SAPE@SPE electrolyte at 0.2C are the same as the low loading cells. The capacity of the LMO//LTO cells in the first several cycles is close to the theoretical capacity of the cell (3 mA h cm^{-1}), which demonstrates a good wetting ability of the SAPE electrolyte into the electrode. Moreover, the UV-cured solid-state aqueous polymer electrolytes have a high mechanical strength and can function as a binder to fabricate a thick electrode in solid state batteries. Remarkably, we demonstrate a thick electrode using UV-cured SAPE as a binder. By mixing LTO with 12m SAPE in the ratio of 1 : 1, and curing under UV light for 90 s, we successfully fabricated the LTO-SAPE electrode with a high loading of 40 mg cm^{-2} and 200 μm thick. The cross-section SEM image of the fabricated LTO-SAPE electrode is presented in Fig. S15 (ESI†). The LTO-SAPE electrode paves the way for the development of high energy solid state battery.

The solid-state aqueous polymer electrolytes provide a technical solution to address the safety problems of lithium-ion batteries and enable a bipolar design of high-voltage and high-energy battery modules. Here, we design a multilayered bipolar cell stacked with 12m SAPE@SPE electrolyte, which avoids the use of some passive components and parts required for packaging and external electrical connection. Hence, the bipolar design facilitates an increase in the volumetric energy density of the battery, while enables easy build-up of high output voltage. Fig. 5c presents the structure of a multilayered bipolar stacked solid-state aqueous polymer electrolyte lithium-ion battery. The bipolar stacked solid-state batteries were fabricated by layering two or three solid-state batteries and trapping them in the CR2032 module coin cell. Fig. 5d shows the voltage profiles of the bi-layered and tri-layered solid-state LMO//LTO full cell at 0.2C. The plateau potential of the bi-layered and tri-layered batteries is 4.9 V and 7.4 V, respectively, which is close to two and three times that of the single-layered battery (2.5 V), confirming that the cell package did not have internal short-circuits and operated successfully.

Conclusions

A solid-state aqueous polymer electrolyte was developed by curing WiSE into the network of methacrylic polymer. The obtained SAPE electrolytes exhibit higher ionic conductivity compared with a traditional solid polymer electrolyte. On comparing the previous reports on ionic liquids, the ion transport properties enhanced with the cooperation of WiSE. The activity of water molecules was further stabilized in the polymer network by the cross-linked solid-state polymer and highly-concentrated salt. A LiF–Li_2CO_3 SEI was formed during the initial charge/discharge cycles, which suppressed water reduction in the following cycles. To further reduce the water reduction in the first few cycles, a water-free thin PEO–LiTFSI–KOH SPE interface was inserted between the anode and electrolyte to further enhance the Coulombic efficiency. The 12m SAPE@SPE electrolyte achieves a wide electrochemical stability window of 3.86 V. The $LiMn_2O_4$//$Li_4Ti_5O_{12}$ full cell with a practical capacity ratio of 1.14 and 12m SAPE@SPE electrolyte exhibited an unprecedented high initial Coulombic efficiency of 90.50% and an average Coulombic efficiency of 99.95% at low 0.5C. The full cell's energy can be enhanced by increasing the active material's area capacity to 1.5 mA h cm^{-1}. A large scale $LiMn_2O_4$/12m SAPE@SPE/$Li_4Ti_5O_{12}$ pouch cell has similar cycle capability with the corresponding coin cell. The pouch cell maintains a high performance after bending with different angles and times, and cutting in air and in water. An ultra-thick LTO electrode with 12m SAPE as binder is also demonstrated as a solid state battery electrode. And a high-voltage (7.4 V) solid-state bipolar cell is assembled with the 12m SAPE@SPE electrolyte. The flexible separator-free SAPE LMO//LTO cells with super robustness can be widely used for low-cost and high-safety flexible electronic devices.

Author contributions

J. Z., C. Y. and C. W. conceived the idea of the study. J. Z., C. C. and P. W. prepared the materials and conducted the electrochemical experiments. Q. L., L. C., F. H., T. J., S. L., N. E., A. C. and L. M. analyzed the data. H. C. and S. R. performed the rhegological test. J. U. and D. A. performed the *in situ* cell pressure and mass spectrometry tests. J. Z., C. C., P. W., C. Y. and C. W. wrote the paper, and all the authors contributed to the interpretation of the results. J. Z., C. C. and P. W. contributed equally to this work.

Conflicts of interest

There are no conflicts to declare.

Acknowledgements

The authors gratefully acknowledge funding support from the US Department of Energy (DOE) through ARPA-E grant (DEAR0000389), U.S. Army Research Laboratory (W911NF1920341) and the Center of Research on Extreme Batteries. We also acknowledge the support of the Maryland Nano Center and its NispLab. The NispLab is supported in part by the NSF as a MRSEC Shared Experimental Facility.

References

1 L. Suo, O. Borodin, T. Gao, M. Olguin, J. Ho, X. Fan, C. Luo, C. Wang and K. Xu, *Science*, 2015, **350**, 938–943.
2 Y. Yamada, K. Usui, K. Sodeyama, S. Ko, Y. Tateyama and A. Yamada, *Nat. Energy*, 2016, **1**, 16129.
3 C. Yang, J. Chen, T. Qing, X. Fan, W. Sun, A. von Cresce, M. S. Ding, O. Borodin, J. Vatamanu, M. A. Schroeder, N. Eidson, C. Wang and K. Xu, *Joule*, 2017, **1**, 122–132.
4 C. Yang, J. Chen, X. Ji, T. P. Pollard, X. Lü, C.-J. Sun, S. Hou, Q. Liu, C. Liu, T. Qing, Y. Wang, O. Borodin, Y. Ren, K. Xu and C. Wang, *Nature*, 2019, **569**, 245–250.
5 G. Xu, X. Shangguan, S. Dong, X. Zhou and G. Cui, *Angew. Chem., Int. Ed.*, 2020, **59**, 3400–3415.
6 L. Suo, O. Borodin, W. Sun, X. Fan, C. Yang, F. Wang, T. Gao, Z. Ma, M. Schroeder, A. von Cresce, S. M. Russell, M. Armand, A. Angell, K. Xu and C. Wang, *Angew. Chem., Int. Ed.*, 2016, **128**, 7252–7257.
7 C. Yang, X. Ji, X. Fan, T. Gao, L. Suo, F. Wang, W. Sun, J. Chen, L. Chen, F. Han, L. Miao, K. Xu, K. Gerasopoulos and C. Wang, *Adv. Mater.*, 2017, **29**, 1701972.
8 Y. Tamai, H. Tanaka and K. Nakanishi, *Macromolecules*, 1996, **29**, 6750–6760.
9 D. Capitani, V. Crescenzi, A. De Angelis and A. Segre, *Macromolecules*, 2001, **34**, 4136–4144.
10 L. T. Ng, J. T. Guthrie, Y. J. Yuan and H. Zhao, *J. Appl. Polym. Sci.*, 2001, **79**, 466–472.
11 E. H. Kil, K. H. Choi, H. J. Ha, S. Xu, J. A. Rogers, M. R. Kim, Y. G. Lee, K. M. Kim, K. Y. Cho and S. Y. Lee, *Adv. Mater.*, 2013, **25**, 1395–1400.
12 Y. H. Chang, C. W. Ku, Y. H. Zhang, H. C. Wang and J. Y. Chen, *Adv. Funct. Mater.*, 2020, **30**, 2000764.
13 C. Decker, *Polym. Int.*, 1998, **45**, 133–141.
14 J. Nair, C. Gerbaldi, G. Meligrana, R. Bongiovanni, S. Bodoardo, N. Penazzi, P. Reale and V. Gentili, *J. Power Sources*, 2008, **178**, 751–757.
15 J. R. Nair, C. Gerbaldi, M. Destro, R. Bongiovanni and N. Penazzi, *React. Funct. Polym.*, 2011, **71**, 409–416.
16 N. Dubouis, P. Lemaire, B. Mirvaux, E. Salager, M. Deschamps and A. Grimaud, *Energy Environ. Sci.*, 2018, **11**, 3491–3499.
17 X. Shen, Y. Li, T. Qian, J. Liu, J. Zhou, C. Yan and J. B. Goodenough, *Nat. Commun.*, 2019, **10**, 1–9.
18 J. M. Klein, E. Panichi and B. Gurkan, *Phys. Chem. Chem. Phys.*, 2019, **21**, 3712–3720.
19 L. Chen, J. Zhang, Q. Li, J. Vatamanu, X. Ji, T. P. Pollard, C. Cui, S. Hou, J. Chen and C. Yang, *ACS Energy Lett.*, 2020, **5**, 968–974.
20 K. Xu, *Chem. Rev.*, 2004, **104**, 4303–4418.
21 D. Lin, W. Liu, Y. Liu, H. R. Lee, P.-C. Hsu, K. Liu and Y. Cui, *Nano Lett.*, 2015, **16**, 459–465.
22 G. Chen, F. Zhang, Z. Zhou, J. Li and Y. Tang, *Adv. Energy Mater.*, 2018, **8**, 1801219.
23 S. Gharazi, B. C. Zarket, K. C. DeMella and S. R. Raghavan, *ACS Appl. Mater. Interfaces*, 2018, **10**, 34664–34673.
24 I. Belharouak, G. M. Koenig, T. Tan, H. Yumoto, N. Ota and K. Amine, *J. Electrochem. Soc.*, 2012, **159**, A1165–A1170.
25 C. Yang, L. Suo, O. Borodin, F. Wang, W. Sun, T. Gao, X. Fan, S. Hou, Z. Ma, K. Amine, K. Xu and C. Wang, *Proc. Natl. Acad. Sci. U. S. A.*, 2017, **114**, 6197–6202.
26 Q. Sun, *Vib. Spectrosc.*, 2009, **51**, 213–217.
27 C. Choe, J. Lademann and M. E. Darvin, *Analyst*, 2016, **141**, 6329–6337.
28 O. Borodin, L. Suo, M. Gobet, X. Ren, F. Wang, A. Faraone, J. Peng, M. Olguin, M. Schroeder, M. S. Ding, E. Gobrogge, A. von Wald Cresce, S. Munoz, J. A. Dura, S. Greenbaum, C. Wang and K. Xu, *ACS Nano*, 2017, **11**, 10462–10471.
29 L. Suo, D. Oh, Y. Lin, Z. Zhuo, O. Borodin, T. Gao, F. Wang, A. Kushima, Z. Wang and H.-C. Kim, *J. Am. Chem. Soc.*, 2017, **139**, 18670–18680.
30 C. Yang, X. Ji, X. Fan, T. Gao, L. Suo, F. Wang, W. Sun, J. Chen, L. Chen and F. Han, *Adv. Mater.*, 2017, **29**, 1701972.
31 A. Shchukarev and D. Korolkov, *Open Chem.*, 2004, **2**, 347–362.
32 L. Zhang, K. Zhang, Z. Shi and S. Zhang, *Langmuir*, 2017, **33**, 11164–11169.
33 J. Ko and Y. S. Yoon, *Ceram. Int.*, 2019, **45**, 30–49.
34 Z. Wu, Y. Wang, X. Liu, C. Lv, Y. Li, D. Wei and Z. Liu, *Adv. Mater.*, 2019, **31**, 1800716.
35 B. Gangaja, K. S. Reddy, S. Nair and D. Santhanagopalan, *ChemistrySelect*, 2017, **2**, 9772–9776.